Article

A Compact C-Band Multiple-Input Multiple-Output Circular Microstrip Patch Antenna Array with Octagonal Slotted Ground Plane and Neutralization Line for Improved Port Isolation in 5G Handheld Devices

Asad Ali Khan [1], Zhenyong Wang [1,2,*], Dezhi Li [1] and Ali Ahmed [3]

1   School of Electronic and Information Engineering, Harbin Institute of Technology, Harbin 150001, China; asadali@stu.hit.edu.cn (A.A.K.); lidezhi@hit.edu.cn (D.L.)
2   Songjiang Laboratory, Harbin Institute of Technology, Harbin 150001, China
3   ACES (Advanced Communications & Electronics Systems), Riyadh 12326, Saudi Arabia; ali.ahmed@aces-co.com
*   Correspondence: zywang@hit.edu.cn; Tel.: +86-137-9615-7286

Abstract: In this paper, an eight-port antenna array is presented for 5G handheld terminals to support multiple-input multiple-output (MIMO) operations. The reported design involves three layers: the top contains eight circular microstrip feed elements; the middle is a low-cost FR-4 substrate, and the bottom layer is a ground plane with four etched octagonal slots. Each resonating element is fed by 50-ohm sub-miniature connectors. To mitigate the detrimental effects of mutual coupling of ports and enhance overall isolation between the adjacent microstrip-fed circular patch elements, a neutralization line is strategically implemented between the feed lines of the antenna array. The design configuration involves two elements at each vertex of the printed circuit board (PCB). The overall dimensions of the PCB are 150×75 mm^2. Each slot and its corresponding radiating elements exhibit linear dual polarization and diverse radiation patterns. The proposed antenna design achieves the required operating bandwidth of more than 1000 MHz spanning from 3 to 4.2 GHz, effectively covering all the upper C-band frequency range of 3.3 GHz to 4.2 GHz allocated for 5G n77 and n78 frequency range 1 (FR1). Required port isolation and lower envelop correlation coefficient (ECC) are achieved for the band of interest. The proposed design gives a peak gain of up to 4 dB for the said band. In addition to these results, degradation in the performance of the antenna array is also investigated during different operating modes of the handheld device. Measured results from the fabricated unit cell and whole array also have a good match with simulated results. On the whole, the proposed antenna possesses the potential to be used in 5G and the open radio access network (ORAN) compliant handheld devices.

Keywords: 5G; handheld devices; antenna array; MIMO; ground slot; neutralization line; high isolation

1. Introduction

Multiple-input multiple-output (MIMO) technology represents a paradigm shift in wireless communications, offering an exponential increase in data transfer rates and spectrum efficiency without necessitating additional transmission power or bandwidth requirements [1]. This groundbreaking approach has emerged as one of the most promising technologies for the 5G communications era [2]. In the realm of cellular communications, the advent of 5G technology has created an urgent demand for low-profile, wideband antenna elements capable of facilitating sufficient mutual coupling within handheld device applications [3–5]. In recent times, numerous designs for MIMO smartphone antennas have been proposed, aimed at catering to the sub-6 GHz frequency range for mobile terminals [6–13]. Recent works such as [14,15] have explored the application of 3D Massive MIMO techniques for enabling high-speed connectivity and massive device support in IoT edge networks and

systems. Ref. [16] addressed the power allocation model in the MIMO-NOMA channel. For MIMO applications, printed antennas have emerged as a favorable choice owing to their cost-effectiveness, ease of fabrication, and inherent capability for seamless integration into compact terminal devices [17]. Slot-coupled antennas have emerged as a prominent choice among researchers for MIMO communication systems across diverse applications, driven by their flexibility in shape design and parameter optimization [18,19]. These antennas, which incorporate slots into conventional antenna structures, have also been leveraged for enabling dual-band operation [20–22]. Slot antennas have garnered substantial research interest over the past several decades due to their applicability across diverse wireless systems, owing to their salient attributes, including a lightweight and compact structure coupled with an inherent facility for integration into radio frequency (RF) circuitry [23]. Notably, the ring-slot antenna topology exhibits the capability to generate two orthogonally polarized radiation modes when excited through distinct feed configurations, a characteristic that has garnered significant attention [8,24]. Researchers are employing neutralization lines in MIMO antenna designs to enhance isolation and mitigate coupling between the antenna elements, a crucial requirement for effective MIMO operation. These neutralization lines, strategically placed between the radiating elements, introduce a phase-opposing current that cancels out the surface currents, thereby decoupling the antenna ports [24–29].

The main objective of this research work is to design a state-of-the-art MIMO antenna on a low-cost substrate for the 5G C-band (3.3–4.2 GHz) with simple design requirements, enhanced isolation, reduced mutual coupling, improved efficiency, and to fulfill the minimum gain requirements and perform well in the operating mode. The designed antenna operates across the 3.3 GHz to 4.2 GHz frequency range, covering the 5G NR Frequency Range 1 (FR1) bands n77 (3.3–4.2 GHz) and n78 (3.3–3.8 GHz). These bands were initially introduced in the 3GPP Release 15 specifications for 5G New Radio (NR), and further enhancements were included in Release 16. The n77 and n78 bands are crucial for providing 5G mobile broadband services in the sub-6 GHz spectrum, enabling high data rates and improved capacity compared to previous generations of cellular technology. The developed antenna's wide operational bandwidth across these bands makes it well-suited for integration into 5G mobile devices, facilitating seamless connectivity and enabling users to leverage the full potential of 5G NR capabilities as defined by the 3GPP standards [30,31].

A CST simulator is used to estimate the key performance indicators of the unit cell and the whole array of the antenna. Section 2 of this paper gives a detailed explanation of the design process, parameters, and working principle of the unit cell. A prototype of the unit cell and also for the eight port array is fabricated to ensure the performance of the antenna. Simulated results are compared and presented for the unit cell. Section 3 explains the design of the 8-port MIMO array for handheld devices. Key MIMO performance indicators like ECC and TARC are taken into consideration. Measured results from the full array fabricated antenna are also compared with the simulated results. A comparison between recently reported 5G mobile phone antennas with the proposed one is presented in Section 4. In the last section, the degradation of the performance of the mobile phone antenna during grip and talk modes in terms of efficiency and gain is presented.

2. Single Unit Two Elements with Slotted Ground Design

This section gives detailed design specifications and working principles of the single unit. The single unit consisted of two circular microstrip edge feed patches designed on a low-cost FR-4 (h = 1.6 mm, ε = 4.3, and δ = 0.025) substrate. The design resonates for the upper C-band (3–4 GHz) with the radiating slot and circular patches, as depicted in Figure 1. The rationale for incorporating a slotted ground plane design and orthogonally positioning the circular patch elements stems from the objective of realizing a dual-polarized antenna system with wideband width and a compact footprint, thereby facilitating seamless integration into the printed circuit board of contemporary smartphone devices. Slot dimensions define resonant frequency; therefore, slot ring circumference needs to fulfill f = c/(λg $*$ L) where f = resonant frequency, c = speed of light in free space,

λg = wavelength, and L = length of one vertex of the slot. The width of the slot and its design affect the impedance bandwidth. Neutralization lines strategically placed within the antenna design can significantly reduce unwanted coupling between ports, improving overall isolation [32]. Detailed design parameters of the single unit are outlined in Table 1. The total dimensions of the antenna are 26 × 26 mm.
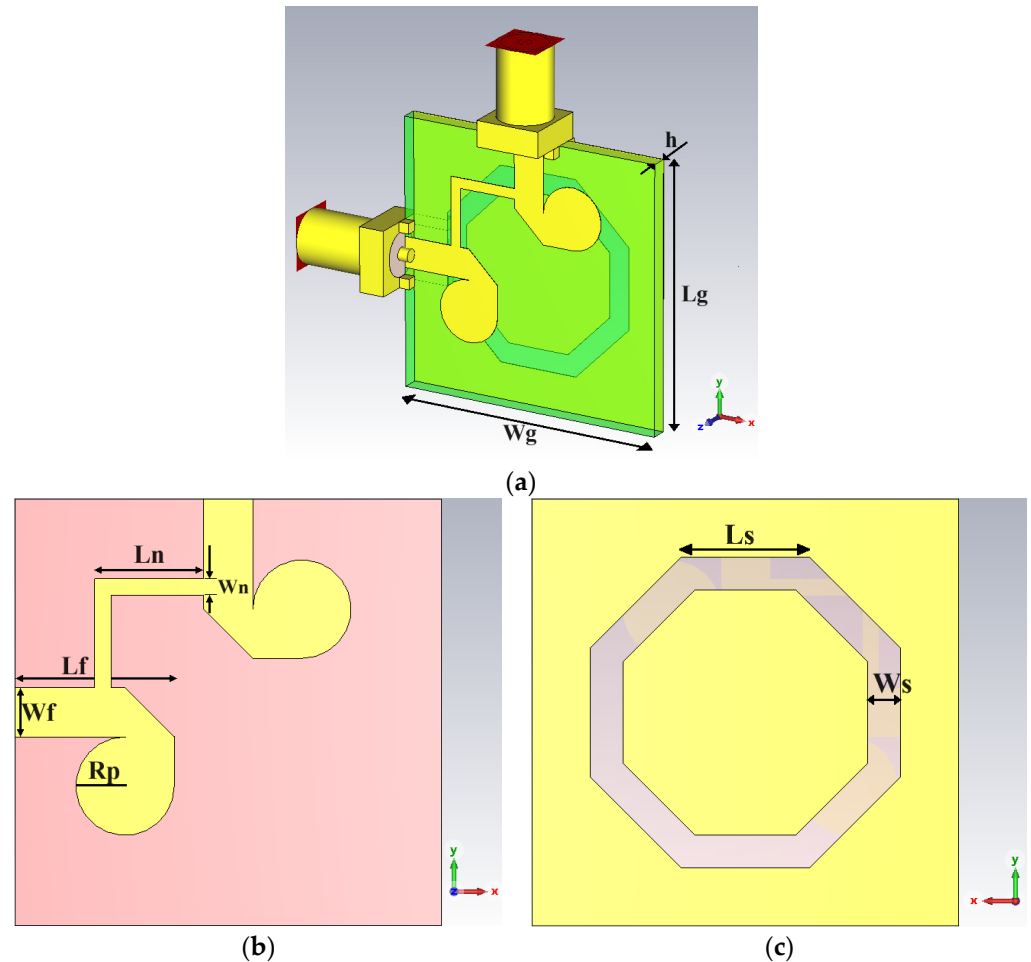

(a)

(b)   (c)

Figure 1. Unit cell design. (**a**) Side View, (**b**) top view, and (**c**) bottom view.

Table 1. Parameter values of the single-element antenna and its MIMO array design.

Parameter	Value (mm)	Parameter	Value (mm)	Parameter	Value (mm)
W	75	Lg	26	Wn	1
L	150	Rp	3	Ln	6.65
h	1.6	Wf	3	Ws	2.17
Wg	26	Lf	9.71	Ls	7.84

The presented single-element antenna design comprised three distinct stages, as illustrated in Figure 2. The design process was initiated with two circular patch antennas employing orthogonal microstrip edge feeding configurations, realized on an FR-4 substrate (height = 1.6 mm, relative permittivity = 4.3) and coupled with a rectangular slot introduced in the ground plane to achieve an impedance bandwidth (3–3.34 GHz) of 340 MHz, overall isolation between −10 and −28 dB, and a peak gain of 2.78 dB. To cover the upper C-Band (3.3–4.2 GHz), we replaced the rectangular slot with an octagonal slot whose width and circumference were carefully optimized for return loss of more than 1 GHz bandwidth, but the isolation and peak gain values remained about the same. In the final stage, to improve isolation, a neutral line was etched between the microstrip feeding lines of both antennas,

and the coupling between both ports decreased by up to −45 dB. The systematic approach for design and optimization was visually represented through the sequential stages and iterative nature of the process. S-Parameters plots, including reflection coefficient and mutual coupling with respective stage design, are shown in Figure 2a–c.
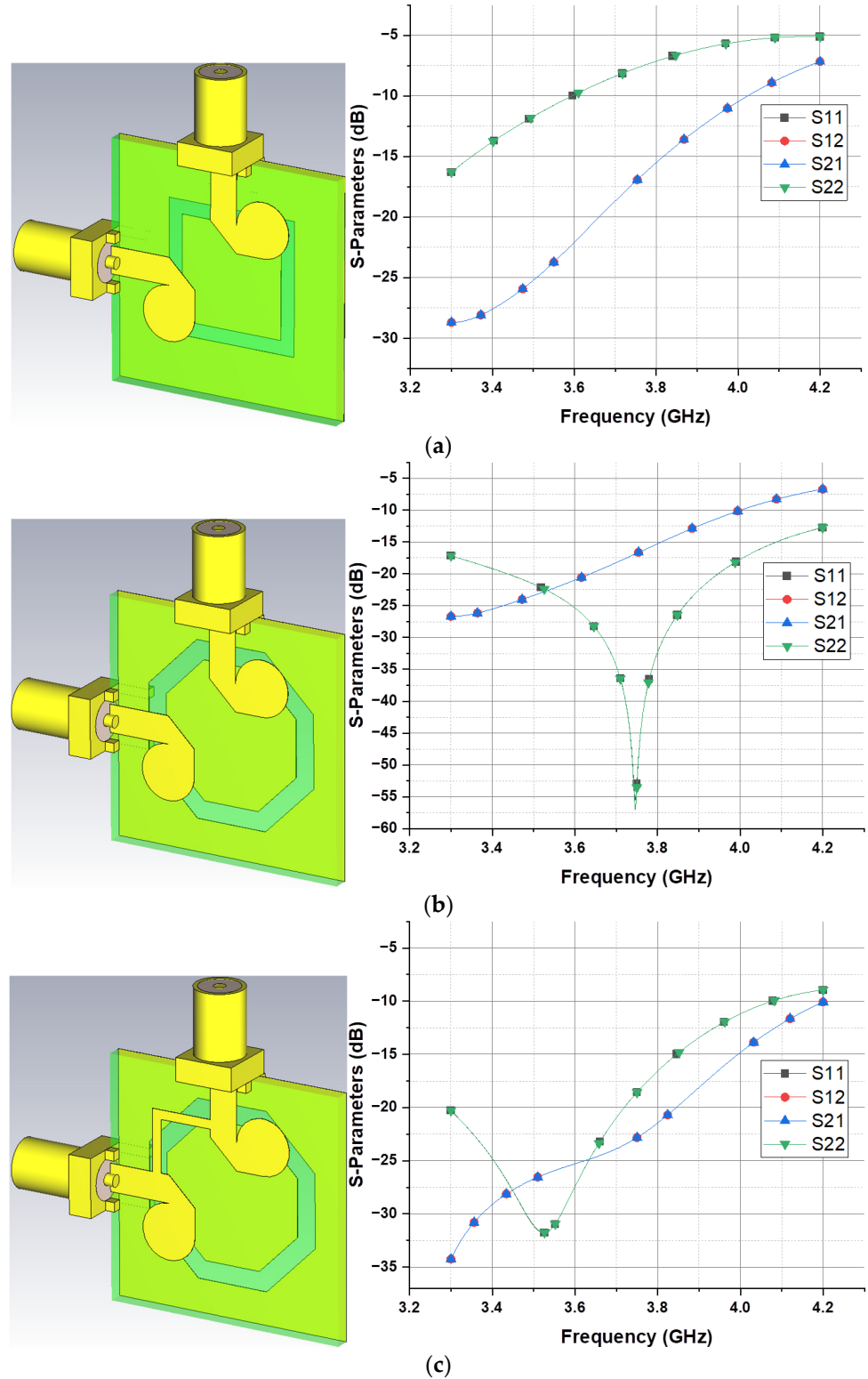

Figure 2. Unit cell design stages with respective S-parameters. (**a**) Stage 1 with rectangular slot, (**b**) Stage 2 with octagonal slot, and (**c**) Stage 3 with neutral line.

The surface current distribution across both ports, as illustrated in Figure 3, exhibited a significant concentration around the radiating elements and the octagonal slot. Notably, the surface current magnitudes on the two ports were equal but opposite in directions, a characteristic attributable to the polarization diversity function [33,34]. This phenomenon arises from the inherent design principles governing the operation of these structures, which facilitate the generation of orthogonally polarized radiation patterns essential for various applications, such as multiple-input multiple-output (MIMO) systems and polarization diversity schemes.
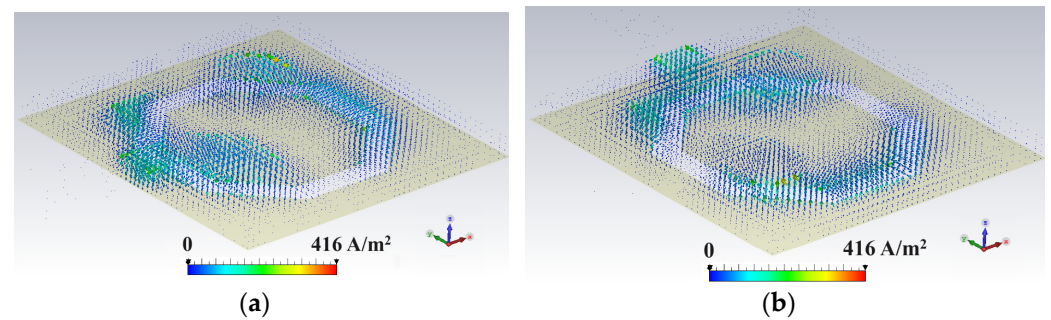

Figure 3. Current densities at 3.5 GHz. (**a**) Port 1, (**b**) Port 2.

The three-dimensional radiation patterns of the proposed antenna, when excited through different feed ports (Port 1 and Port 2), are depicted in Figure 4. As evident from the figure, the antenna exhibited nearly identical radiation characteristics with orthogonally polarized fields. The orthogonally polarized radiation patterns exhibited by the antenna when excited through different feed ports are an inherent characteristic stemming from its polarization diversity design. This polarization diversity capability can prove advantageous for handheld wireless communication applications, where it plays a crucial role in enhancing data traffic performance. In such scenarios, polarization diversity is essential as it mitigates the effects of polarization mismatch, improves the signal-to-noise ratio, and provides robustness against multipath fading, thereby ensuring reliable and high-quality data transmission [6,35,36]. Furthermore, the radiation patterns exhibited a peak gain of approximately 3 dBi. The radiation performance metrics, encompassing radiation efficiency, total efficiency, and maximum gain, for the proposed dual-polarized octagonal-ring slot antenna are quantified in Figure 5, providing comprehensive insights into its radiation characteristics. An examination of the results reveals that the antenna exhibited total and radiation efficiency levels exceeding 85% across nearly the entire operational bandwidth of interest, i.e., 3.3–4.2 GHz. Furthermore, the antenna achieved a commendable peak directivity of 3.4-dB.
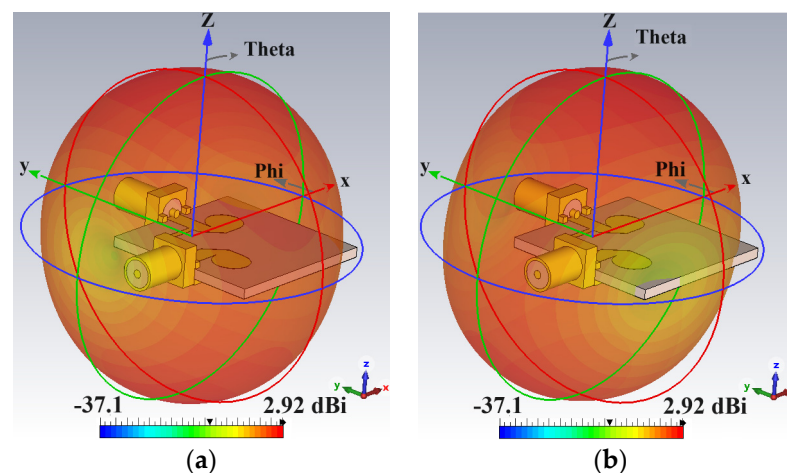

Figure 4. 3D dual polarized radiation pattern of orthogonal elements. (**a**) Port 1, (**b**) Port 2.
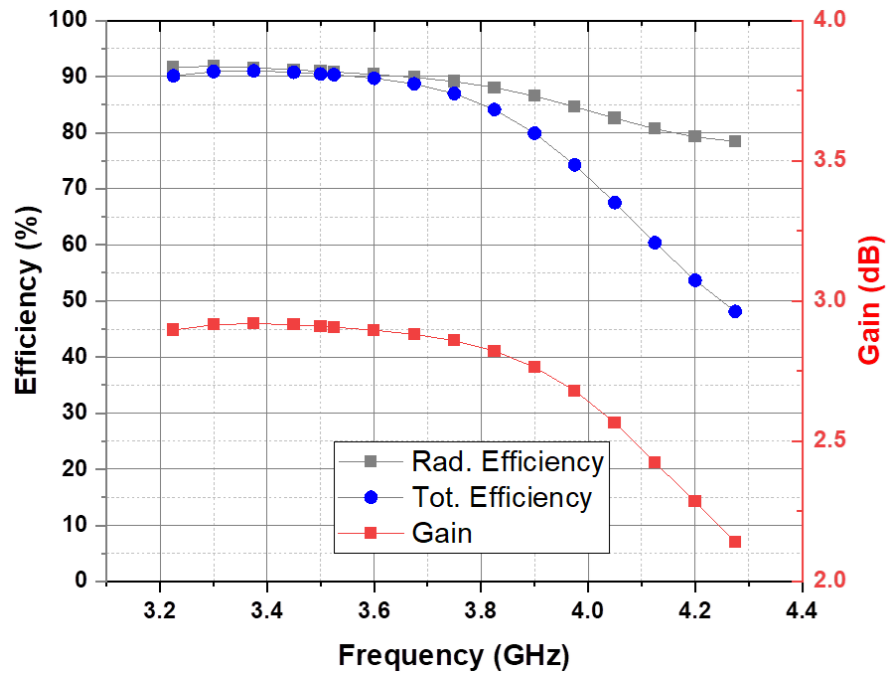
Figure 5. Radiation efficiencies, Total efficiencies, Maximum gain of the unit cell of the MIMO antenna.

To validate the proposed design, a prototype of the antenna was fabricated, and its S-parameters were experimentally characterized. Figure 6 presents a photograph of the fabricated prototype integrated into the measurement setup. The measured and simulated S-parameter results, including reflection coefficient and mutual coupling for the fabricated antenna, are depicted in Figure 7. A close agreement between the measured and simulated results can be observed, corroborating the proper operation of the fabricated antenna across the desired frequency range.
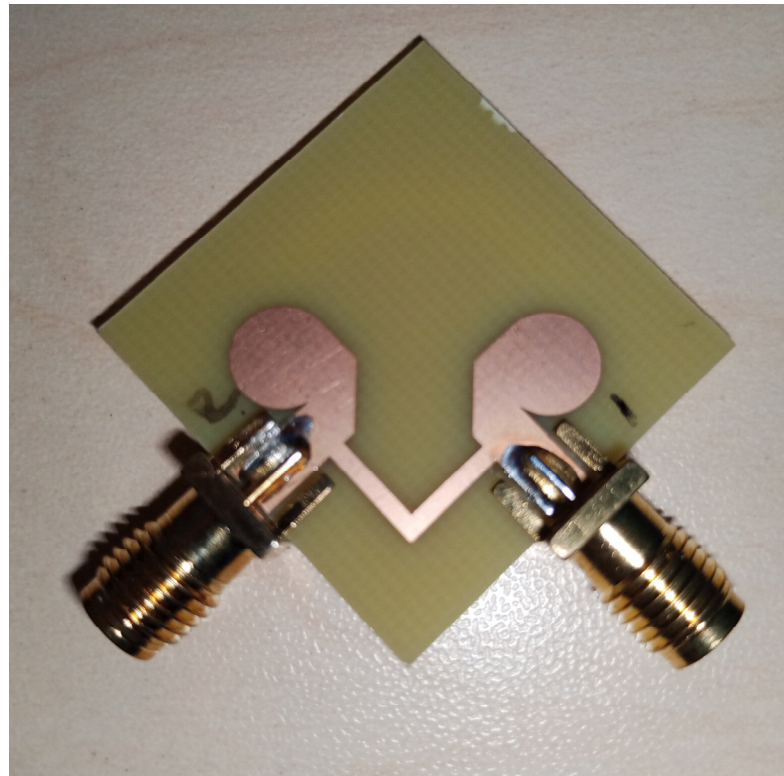

Figure 6. Visuals of the unit cell during measurement of S-parameter.
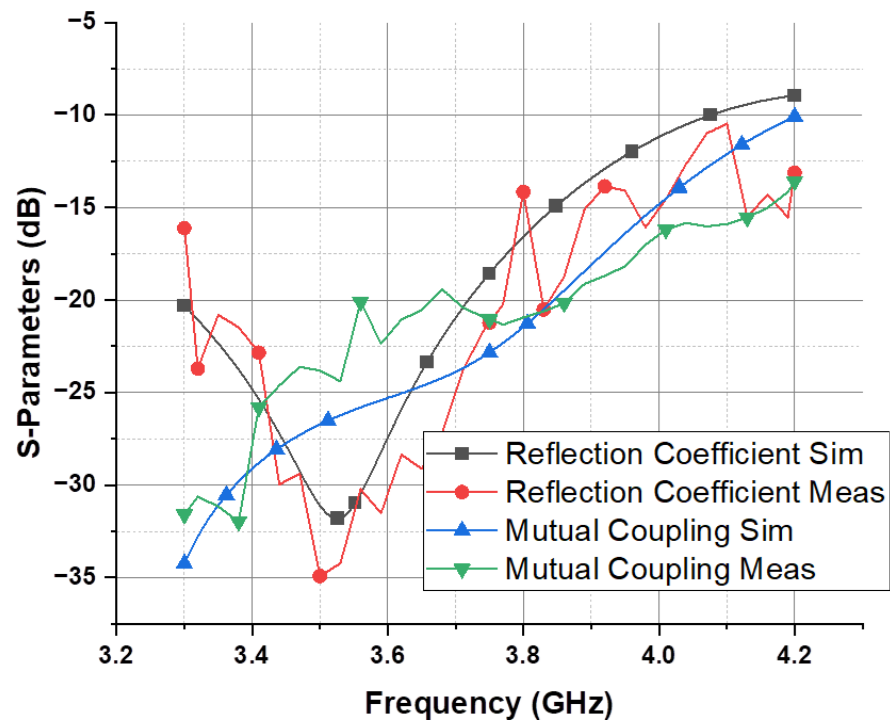
Figure 7. Comparison of measured and simulated S-parameter.

### 3. 8-Port MIMO for Handheld Devices Antenna Design

Figure 8 presents the complete layout of the proposed MIMO antenna for handheld mobile devices. An FR-4 substrate (h = 1.6 mm, ε = 4.3, and δ = 0.025) with dimensions of 150×75 mm^2 was used to implement the design. Eight resonating antenna elements fed four octagonal-ring slot radiators, each at the vertex of the mobile printed circuit board. Antenna elements were placed in such an arrangement to give a dual polarization effect. It is evident from the configuration that the compact size of the employed radiator elements allows for sufficient available space on the smartphone antenna PCB to accommodate additional antennas operating at other different frequency bands. This modular approach facilitates the integration of multiple radiating elements within the confines of the mobile device, thereby enabling the coverage of diverse wireless communication standards and frequency allocations.

Figure 9 illustrates the s-parameter for the reflection coefficient and also for isolation. The results obtained underscore the favorable performance characteristics of the proposed mobile phone antenna design, exhibiting commendable S-parameter response with a wide operational bandwidth covering FR-1 n77, n78 (3.3–4.2 GHz), and low mutual coupling between the radiating elements. These attributes are highly desirable for efficient and reliable wireless communication in mobile devices, as they facilitate robust signal transmission and reception while mitigating potential interference and signal degradation.

Figure 10 illustrates the three-dimensional radiation patterns of two adjacent antenna elements designated as Antenna 1 and Antenna 2 at a frequency of 3.5 GHz. A noteworthy observation from the radiation patterns is the coverage provided by the antenna across the top and bottom regions of the mobile device, a desirable characteristic for ensuring reliable wireless connectivity in various orientations and usage scenarios.
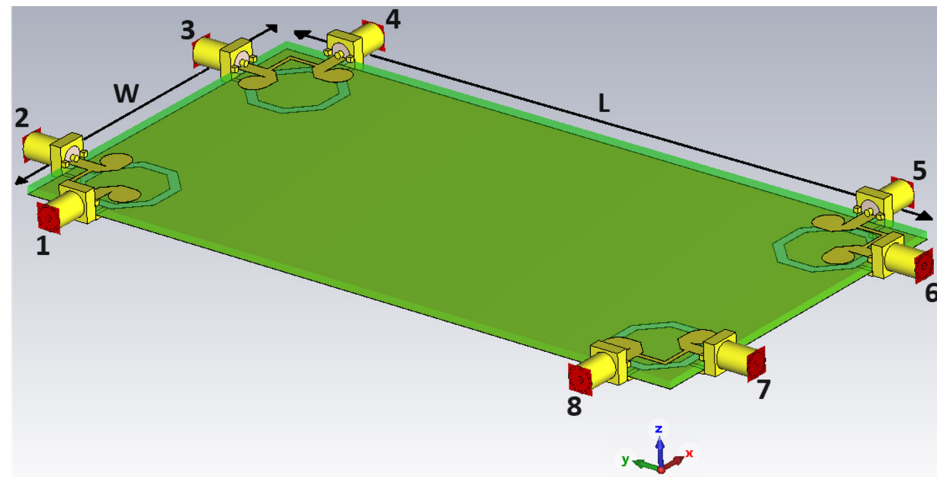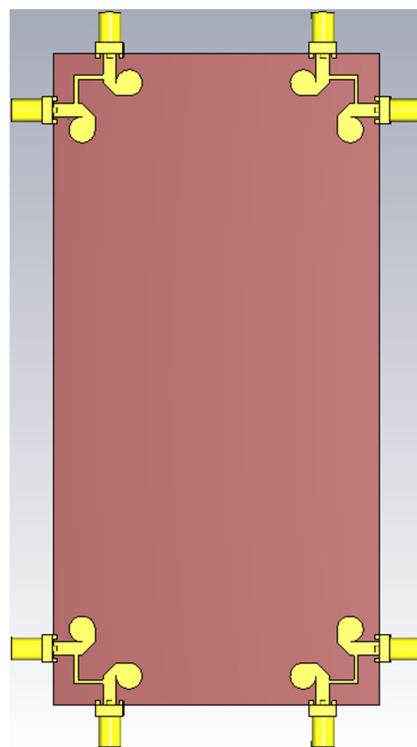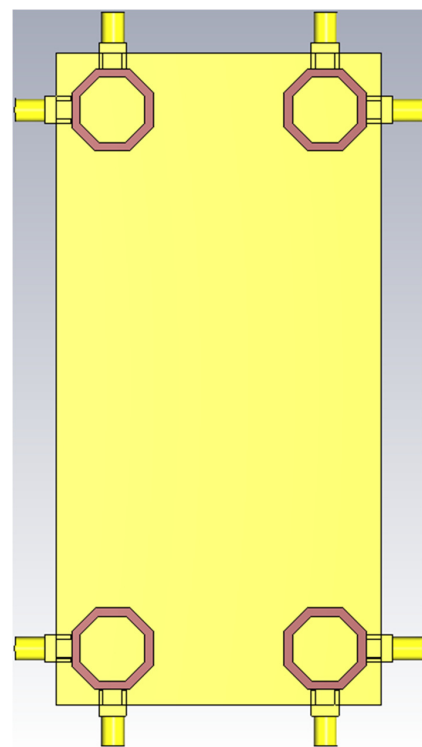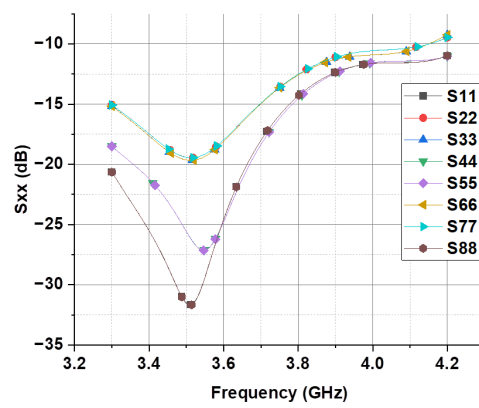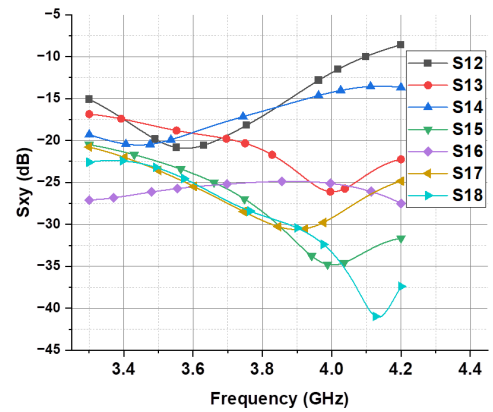
Figure 8. Handheld device antenna design. (**a**) Side view, (**b**) top view, and (**c**) bottom view.

Figure 9. S-parameter values of 8-port array. (**a**) Reflection coefficient, (**b**) mutual coupling.
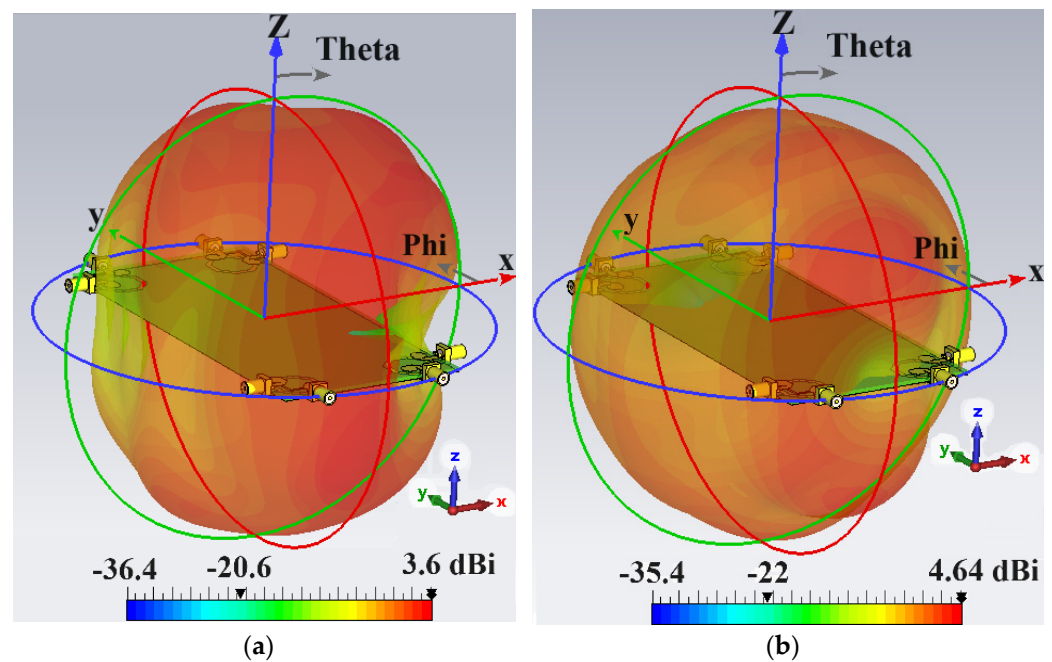
Figure 10. 3D radiation pattern of adjacent elements. (**a**) Port-1, (**b**) Port-2.

The radiation characteristics of the proposed mobile phone antenna design were further elucidated through the top-view radiation patterns depicted in Figure 11. It is evident that each lateral aspect of the mobile phone printed circuit board (PCB) was encompassed by radiation patterns exhibiting distinct polarization orientations. This attribute enabled the multiple-input multiple-output (MIMO) antenna system to achieve comprehensive radiation coverage while simultaneously supporting diverse polarization states. Consequently, the presented antenna design exhibits enhanced suitability for future wireless communication applications that demand robust performance and adaptability to varying propagation environments and device orientations. Moreover, the antenna exhibited commendable gain, radiation, and total efficiency performance for four ports, each from a separate unit, across the operational frequency band, as exemplified in Figure 12. The efficiencies of both ports of a single unit were the same due to symmetry in normal mode. Notably, the radiating elements achieved radiation and total efficiencies exceeding 80% at the 3.5 GHz frequency band. This high-efficiency characteristic is a testament to the optimized design and minimization of potential losses, thereby ensuring effective electromagnetic radiation and transmission of the desired signal power. Such efficiency metrics are crucial for enabling reliable and energy-efficient wireless communication in mobile devices, contributing to enhanced battery life and overall system performance [6].

To validate the proposed design, a prototype of the mobile phone antenna was fabricated, and its performance characteristics were experimentally evaluated at the Antenna Laboratory facilities of the prestigious Harbin Institute of Technology. Figure 13 provides top and bottom view illustrations of the fabricated prototype, respectively. The availability of these physical prototypes facilitated comprehensive testing and measurement procedures, enabling the corroboration of the antenna's simulated performance against empirical data obtained under controlled laboratory conditions. The mobile phone antenna prototype was constructed on an economical FR-4 dielectric substrate, with an overall compact dimension of $75 \times 150 \times 1.6$ mm^3. During the experimental measurement process, 50-Ω radio frequency (RF) loads were strategically employed for the radiating elements that were not under evaluation. This precautionary measure aimed to mitigate potential undesirable effects and interference from the inactive elements, ensuring accurate and reliable characterization of the element undergoing testing.
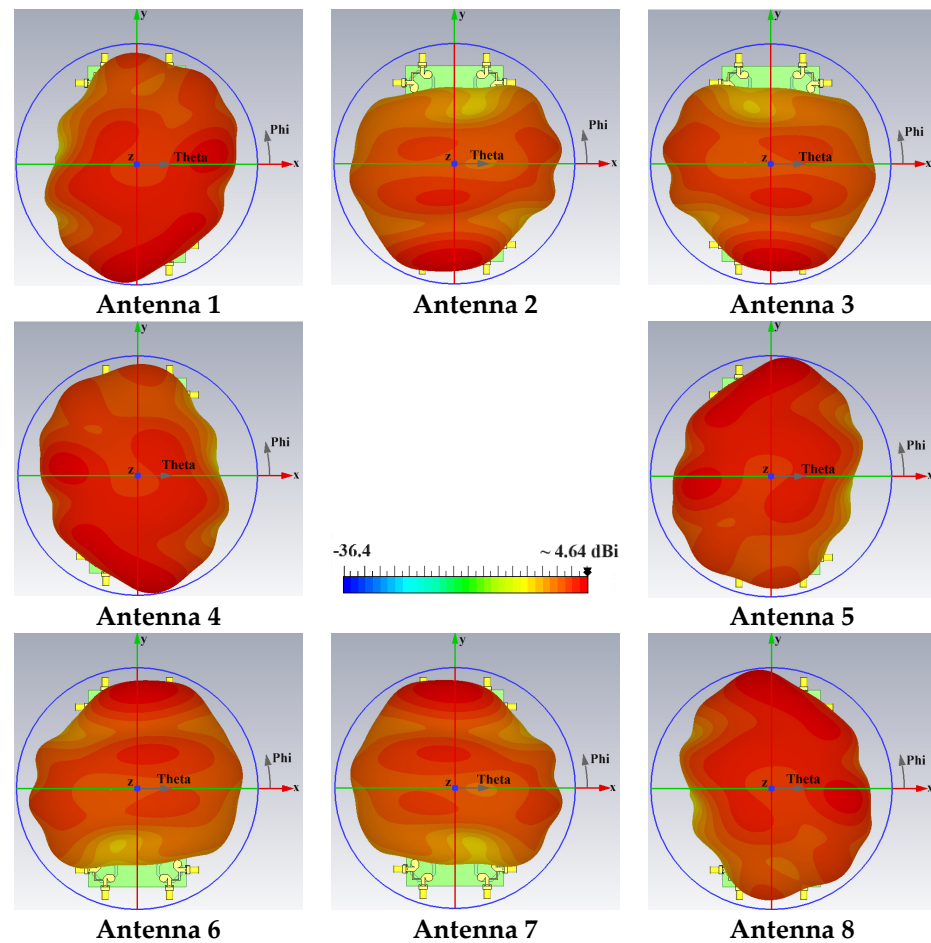
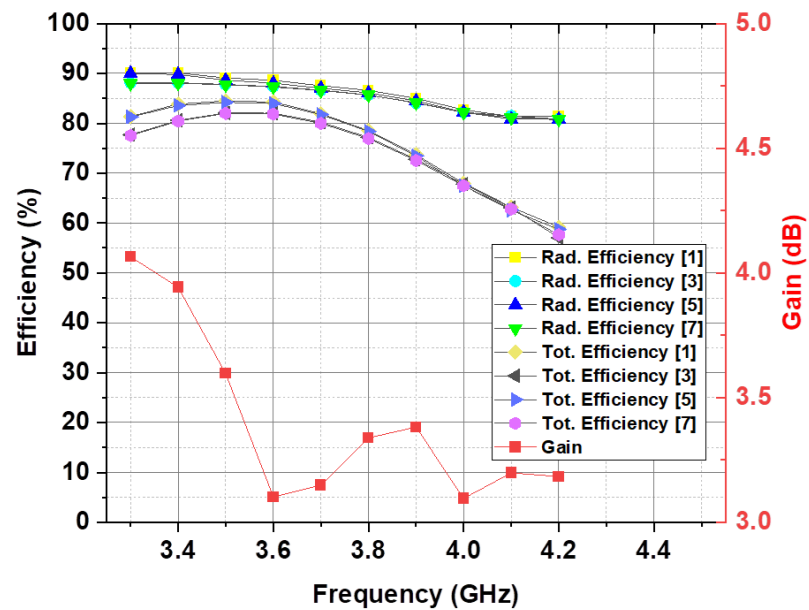**Figure 11.** 3D radiation pattern of each antenna array.

Figure 12. MIMO antenna gain, radiation, and total efficiencies of Ports 1, 3, 5, and 7 each from separate unit.
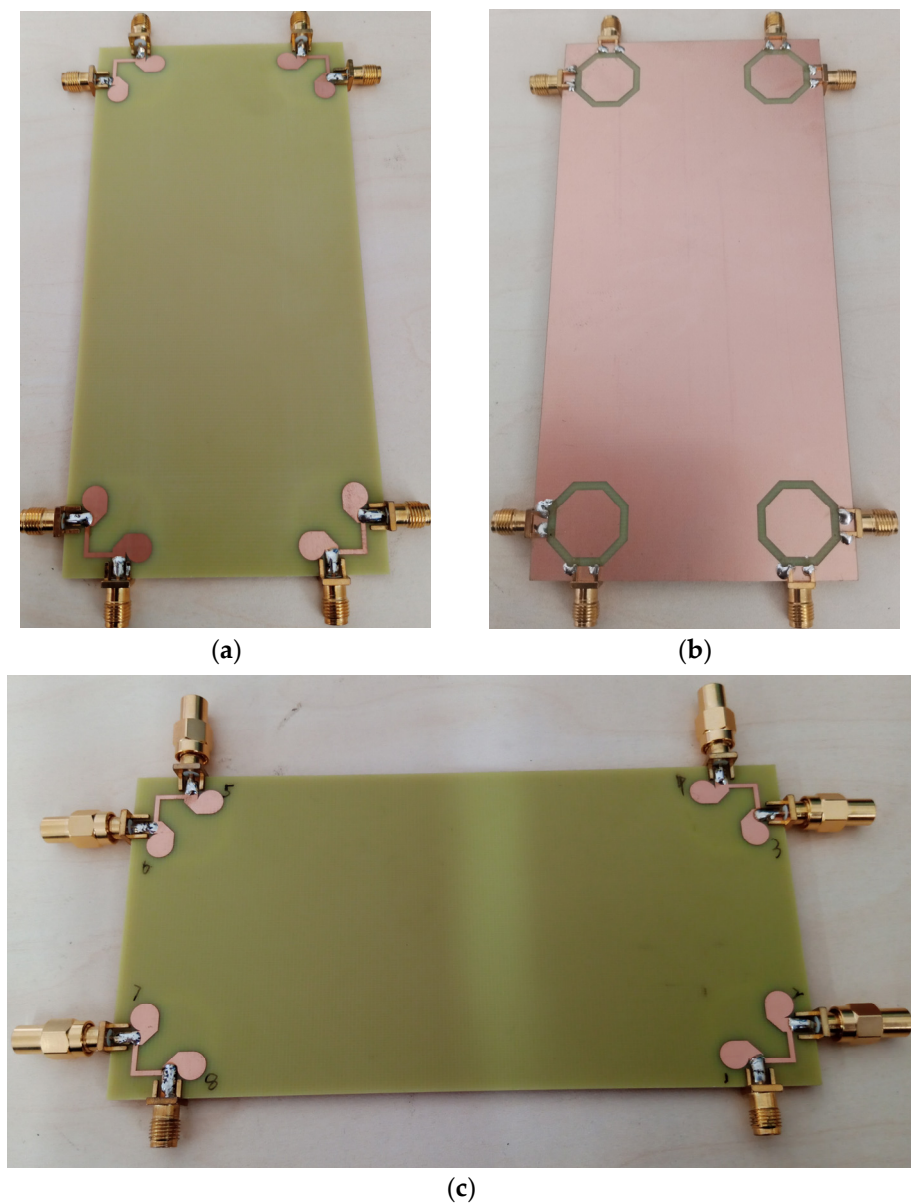
(a)

(b)

(c)

Figure 13. Fabricated antenna. (**a**) Top view, (**b**) bottom view, and (**c**) s-parameter measurement setup with 50-Ω load.

Figure 14 depicts the measured and simulated S-parameter reflection coefficients and mutual coupling characteristics of the fabricated antenna design. As evidenced by the results, the octagonal-ring slot resonators exhibited favorable S-parameter performance, characterized by adequate impedance bandwidth and low mutual coupling levels across the desired frequency range. The remarkable port isolation demonstrated in Figure 15 can be attributed to the antenna's innovative design, which incorporated a neutralization line technique. This strategic incorporation yielded commendable performance, as evidenced by the clear comparison presented in the figure. It is worth noting that minor deviations between the measured and simulated results can be ascribed to potential inaccuracies introduced during the fabrication process, feed assembly, and experimental procedures. Nonetheless, the overall agreement between the measured and simulated data validates the efficacy of the proposed design and its suitability for the intended application.
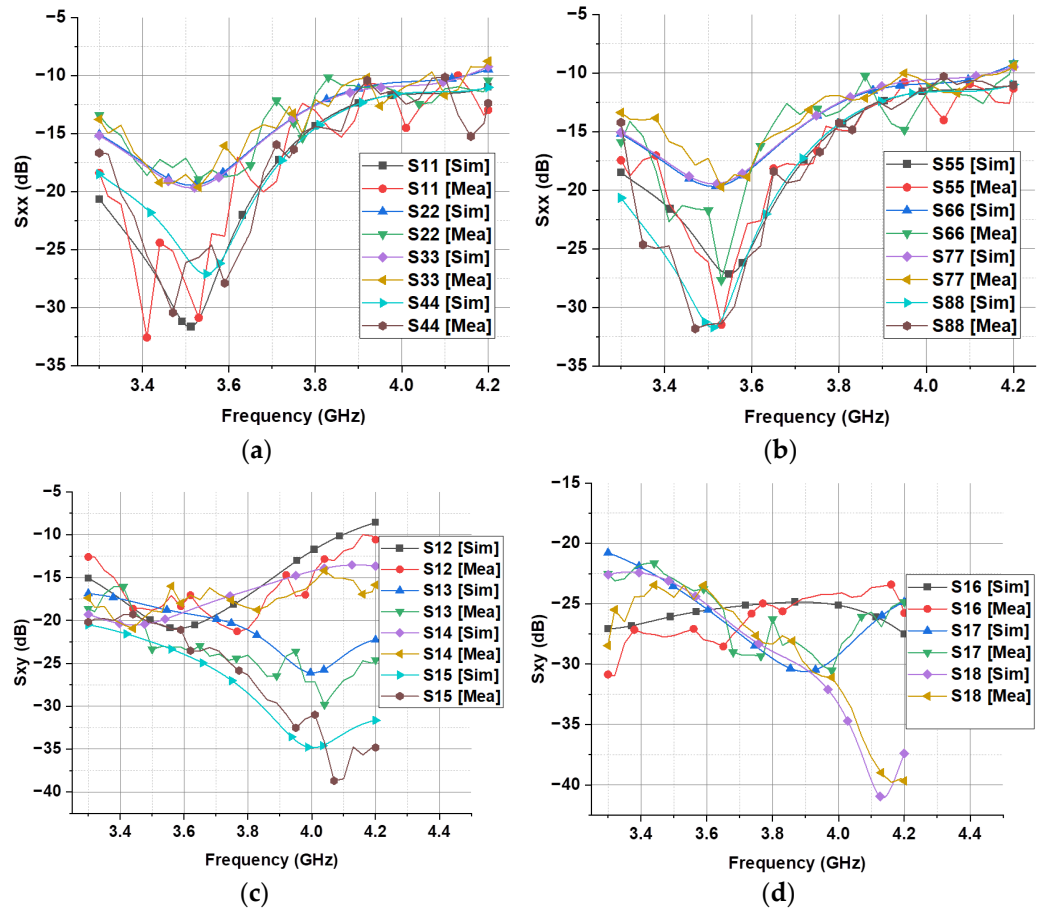
Figure 14. Comparison between simulated and measured results for the (**a**) first four port reflection coefficient, (**b**) last four port reflection coefficient, and (**c**,**d**) mutual coupling.
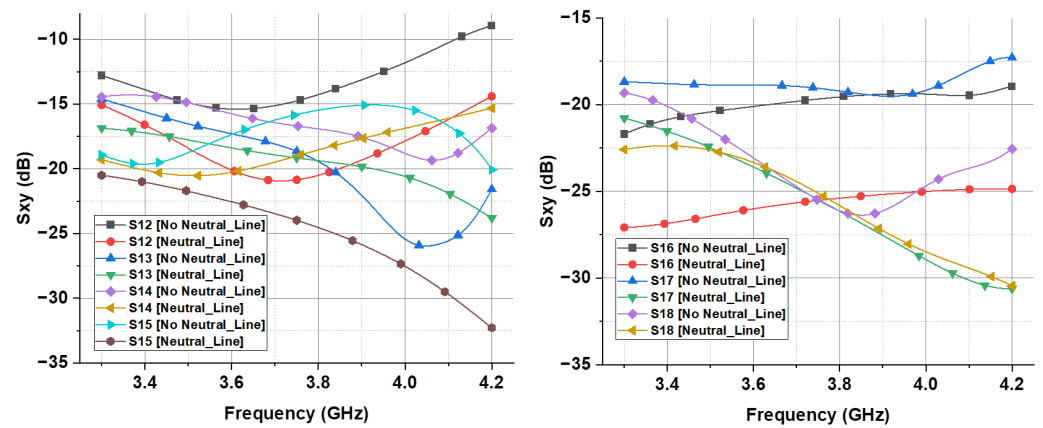

Figure 15. Comparison of port isolation with and without neutral line.

Considering the premise that radiation elements with identical placements and polarizations exhibit similar radiation patterns, two-dimensional polar radiation patterns of the adjacent resonators (encompassing Ant. 1 and Ant. 2) were experimentally measured at the central operating frequency of 3.5 GHz. The results are depicted in Figure 16. As evidenced by the measurements, the fabricated prototype exhibited favorable radiation pattern characteristics, demonstrating acceptable agreement with the simulated results. Moreover, the antenna elements with orthogonal polarizations provided sufficient gain values at the center frequency of the operational band. This performance validation substantiates the

efficacy of the proposed design and its ability to meet the specified radiation requirements, further underscoring its suitability for the intended wireless communication applications.
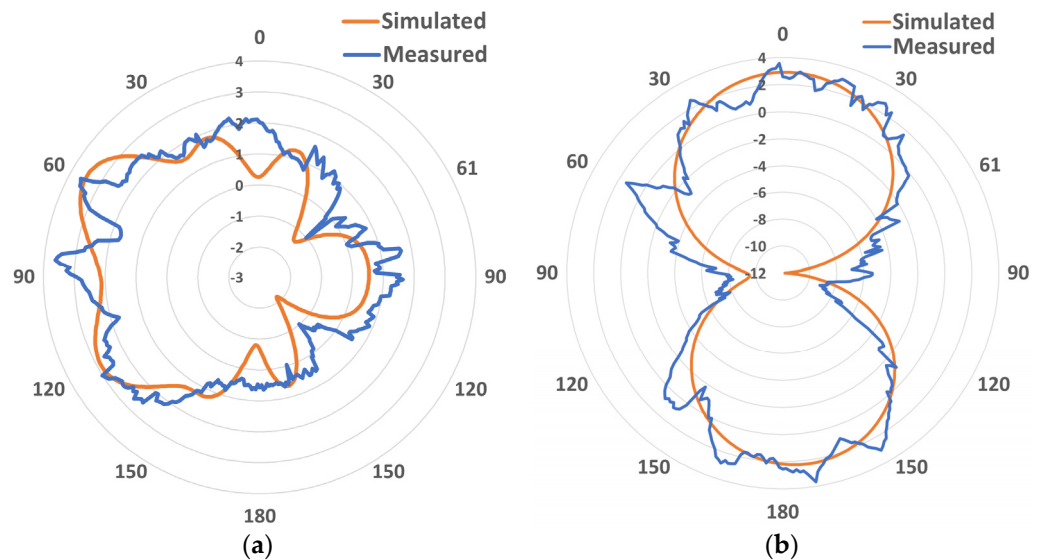

Figure 16. Simulated and measured 2D radiation patterns for (**a**) Antenna.1 and (**b**) Antenna.2.

In the context of multiple-input multiple-output (MIMO) antenna systems, it is imperative to evaluate the envelope correlation coefficient (ECC) and total active reflection coefficient (TARC) characteristics to ensure proper functionality. These parameters play a crucial role in assessing the performance of MIMO antennas. The ECC and TARC values for the radiating elements can be derived from the measured S-parameters using well-established mathematical formulations described in the literature. These calculations provide quantitative insights into the correlation between the antenna elements and their active reflection coefficients, respectively, enabling a comprehensive assessment of the MIMO antenna's suitability for practical applications. The following equations were used to calculate ECC and TARC values [7,37].

$$\text{ECC} = \frac{|S_{mm}^* S_{nm} + S_{mn}^* S_{nn}|^2}{\left(1 - |S_{mm}|^2 - |S_{mn}|^2\right)\left(1 - |S_{nm}|^2 - |S_{nn}|^2\right)^*} \tag{1}$$

$$\text{TARC} = -\sqrt{\frac{(S_{mm} + S_{mn})^2 + (S_{nm} + S_{nn})^2}{2}} \tag{2}$$

Figure 17 illustrates the calculated envelope correlation coefficient (ECC) and total active reflection coefficient (TARC) results derived from the simulated S-parameters of the proposed mobile phone antenna design. As evident from the figures, the calculated ECC and TARC values exhibited remarkably low magnitudes across the entire operating frequency band of interest. Notably, the design achieved an ECC lower than 0.017 throughout the operational bandwidth, indicating negligible correlation between the two adjacent radiating elements. Furthermore, the TARC value was less than -44 at the central frequency of 3.5 GHz, underscoring the antenna's favorable active reflection characteristics.

Table 2 provides a comprehensive summary and comparison of the fundamental performance metrics of the presented mobile phone antenna design against other reported 5G mobile phone antenna designs [9–13,38]. It is evident that the proposed design offers superior performance in terms of efficiency, isolation, and ECC. Additionally, it exhibited a wider operational bandwidth while incorporating pattern and polarization diversity characteristics, enabling comprehensive coverage across the various lateral aspects of the mobile phone printed circuit board (PCB). These attributes collectively underscore the suitability of the presented antenna design for next-generation wireless communica-

tion applications, offering enhanced performance, reliability, and adaptability to diverse propagation environments and device orientations.
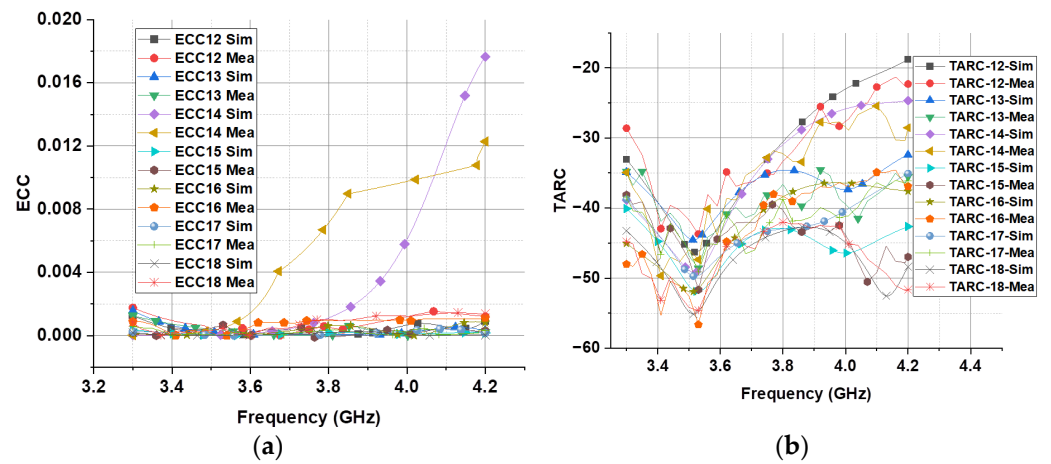

Figure 17. Comparison of simulated and measured results for (**a**) Envelope correlation coefficient (ECC) and (**b**) total active reflection coefficient (TARC).

**Table 2.** Comparison between the presented and recently reported 5G mobile phone antennas.

Ref. #	Bandwidth	Element	Efficiency	Size	Peak Gain	Isolation	ECC
[9]	3.4–3.6 (−6 dB)	8	42–65	150 × 70	2.87	12	<0.2
[10]	3.4–3.6	8	62–76	150 × 75	N/A	12	<0.05
[11]	3.55–3.65	4	52–76	150 × 75	N/A	11	N/A
[12]	3.4–3.6	8	60–75	150 × 80	N/A	17	<0.05
[13]	3.3–3.7 (−6 dB)	8	50–70	136 × 68	4	15	0.1
[38]	3.45–3.55 (−6 dB)	4	40–50	120 × 73	1.9	15	<0.31
Proposed	3.3–4.2	8	80–88	150 × 75	4	21	<0.017

## 4. Effect on Antenna Array Performance during Operational Modes

In this section, the influence of the human hand and human head on the performance characteristics of the proposed design was rigorously examined, specifically analyzing their impact on the total efficiency and realized gain of the antenna. This investigation was conducted in accordance with established methodologies and guidelines outlined in the relevant literature [8,37]. To thoroughly evaluate the performance implications, comprehensive simulations were conducted encompassing diverse operational scenarios. Specifically, as depicted in Figure 18, the study investigated the effects of right-hand and left-hand grip modes on the total efficiencies of ports for both the top-layer and back-layer configurations of the proposed design. The simulation results demonstrated that the proposed mobile phone antenna design and its radiating elements exhibited robust performance characteristics and maintained satisfactory total efficiency across all eight ports of the antenna, even in the presence of the human hand. Owing to the inherent symmetry of the proposed configuration, the antenna exhibited consistent performance across the various hand grip scenarios investigated. The most significant reductions in radiation properties were observed in cases where the radiating elements were partially obstructed by the user's hand. This phenomenon can be attributed to the intrinsic dielectric properties of human tissue, which can lead to substantial absorption of radiated power.

(**a**)

(**b**)
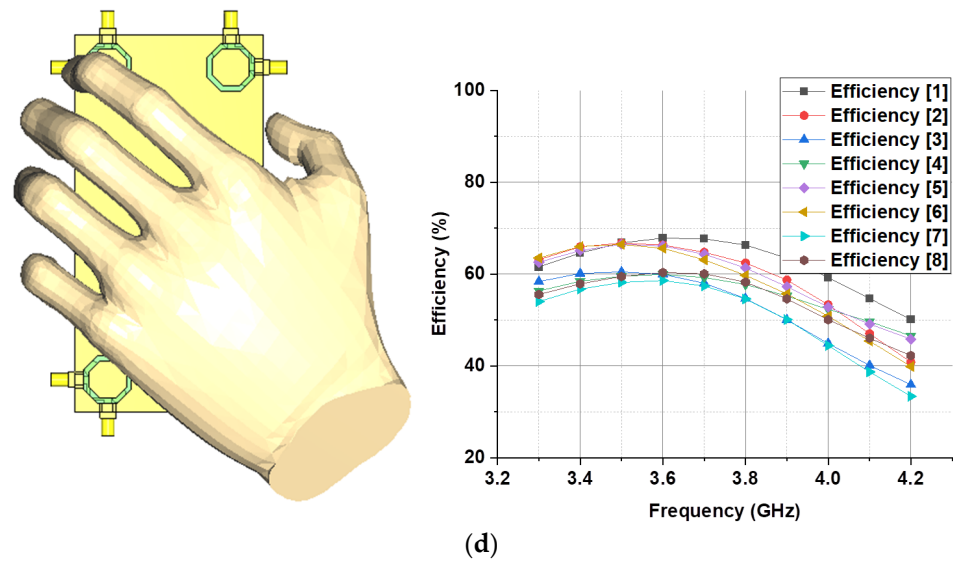

(**c**)

Figure 18. *Cont.*

(d)
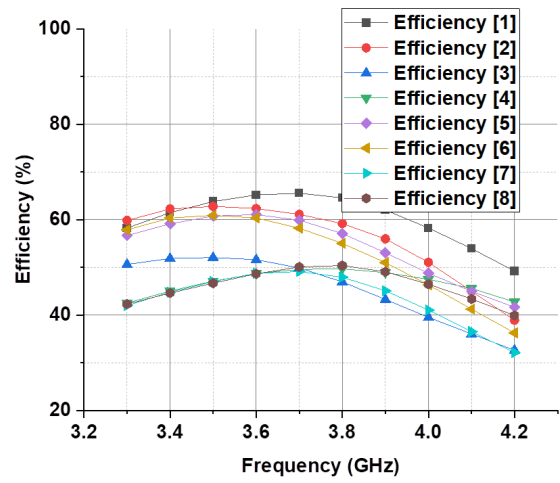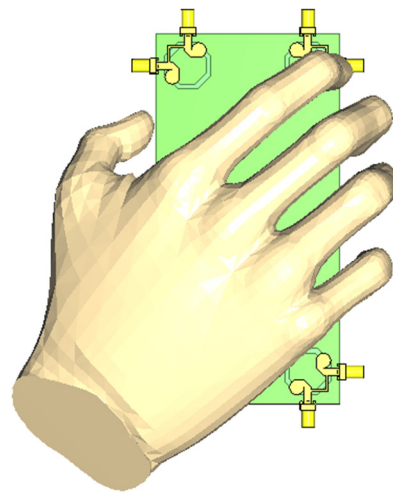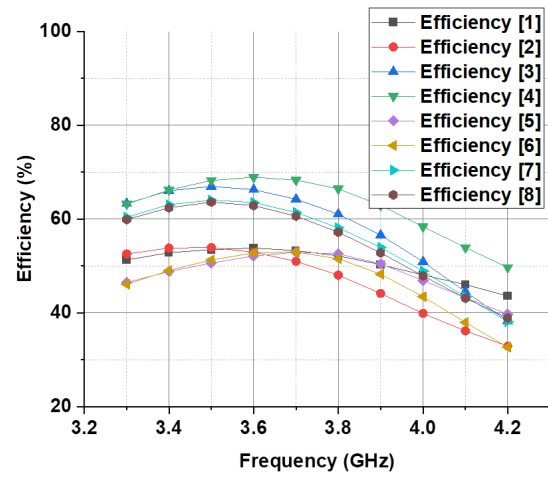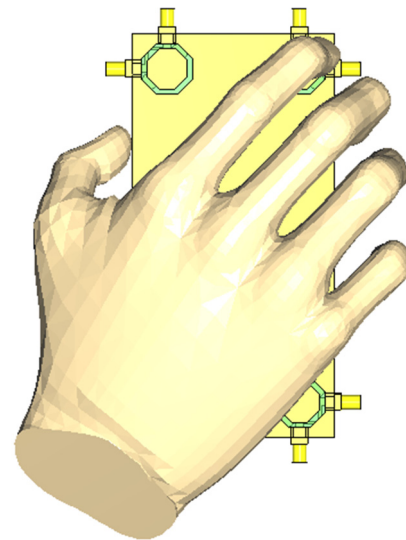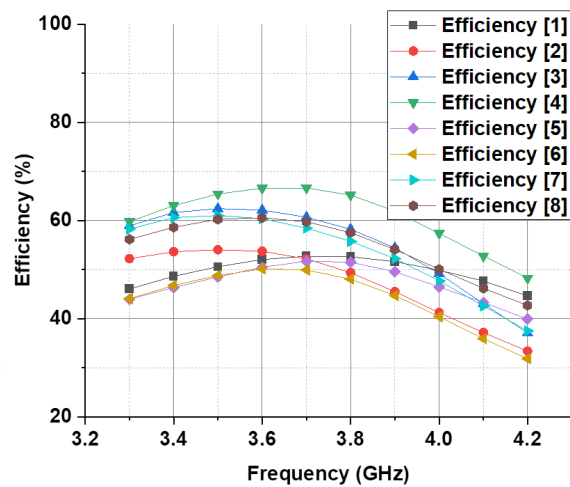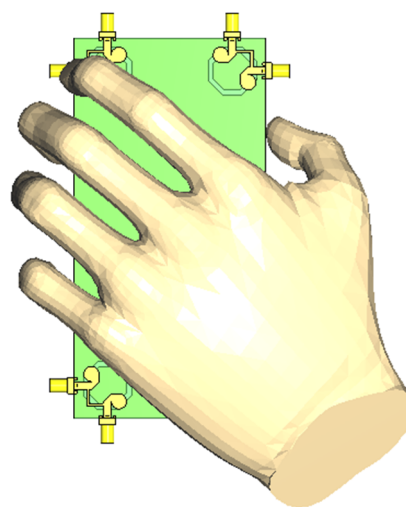
Figure 18. Effect of human grip on total efficiencies of eight ports of the antenna. (**a**) Right-hand top layer, (**b**) right-hand bottom layer, (**c**) left-hand top layer, and (**d**) left-hand bottom layer.

Figure 19 depicts the three-dimensional radiation patterns of the mobile phone antenna while operating in the Talk-Mode scenario at a frequency of 3.6 GHz. It is noteworthy that the radiation performance of each individual antenna element was primarily contingent upon its spatial positioning within the Talk-Mode configuration. As illustrated, the realized gain characteristic of the design exhibited variations spanning the range of 2.5 to 3.5 dB. In comparison to the radiation patterns observed in free-space conditions (Figure 11), the presence of the user's head and hand introduced distortions and attenuation in the radiation patterns. This phenomenon can be attributed to the partial obstruction of the antenna elements by various segments of the hand and head phantoms, as evident in the presented Talk-Mode configuration.

Figure 20 presents the total efficiency and reflection coefficient characteristics of the antenna elements when operating in the Talk-Mode scenario, in the presence of the user's head and hand. As illustrated, the deviation in the S-parameter performance of the design was negligible. Furthermore, the proposed MIMO configuration exhibited satisfactory efficiency levels across its operational bandwidth. Based on the comprehensive analysis conducted, it can be concluded that the MIMO design demonstrates adequate efficiency, radiation coverage, and gain performance, rendering it a viable candidate for handheld antenna applications.
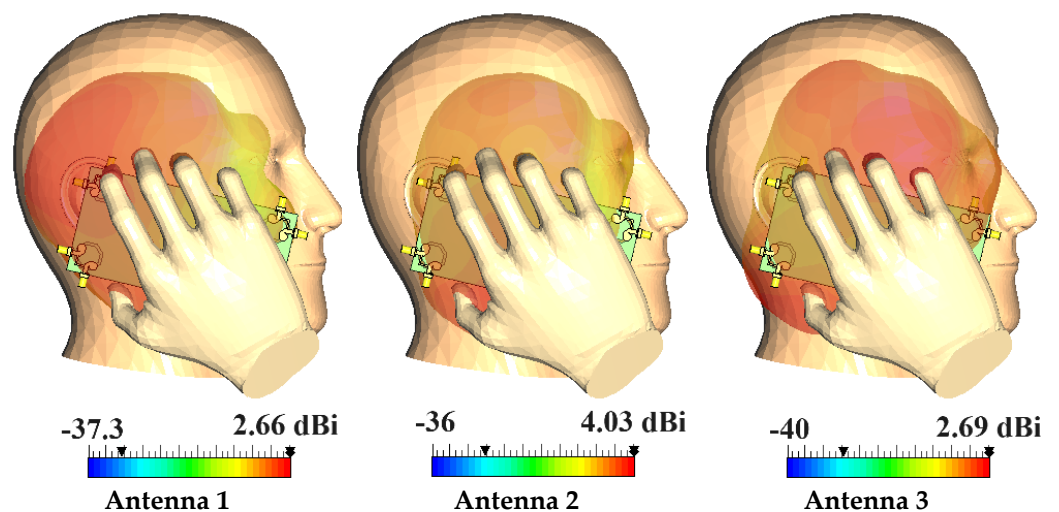
Figure 19. *Cont.*
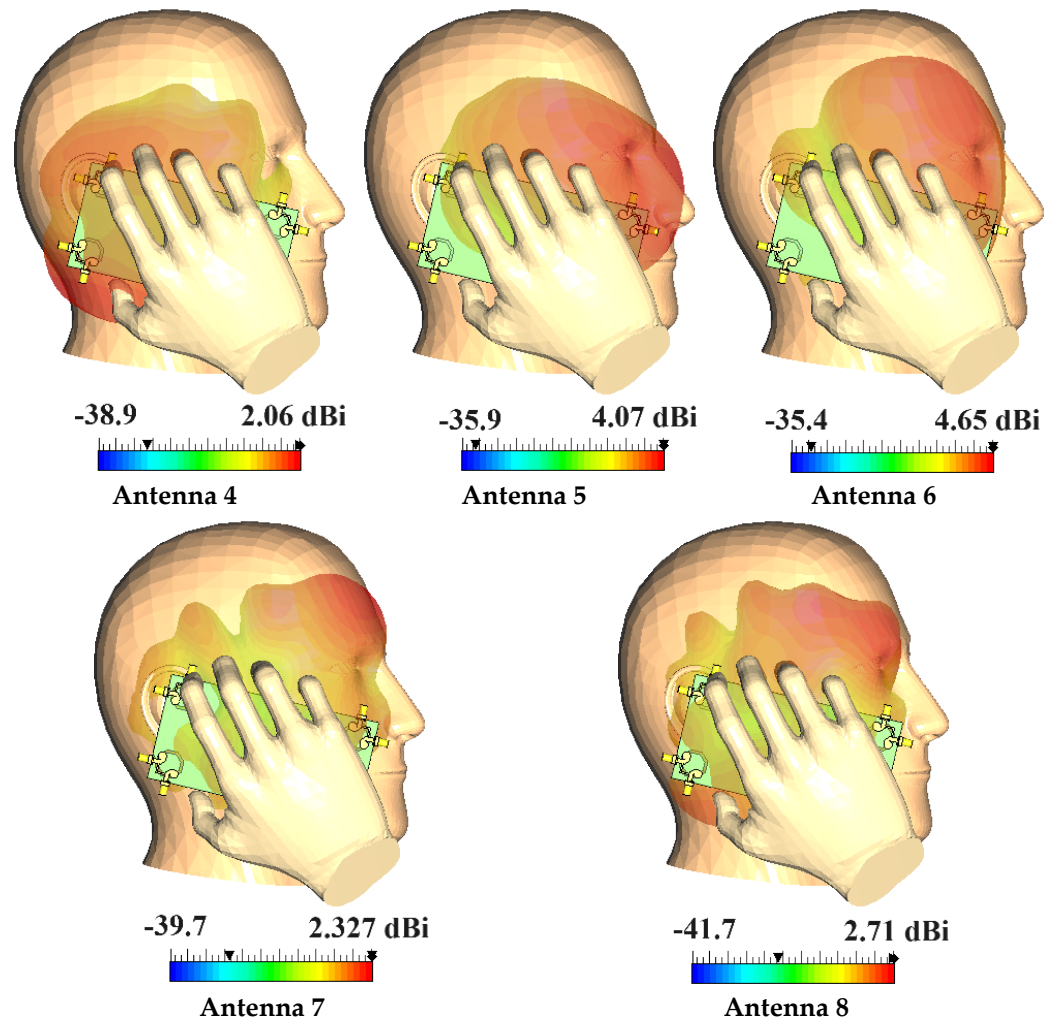
Figure 19. 3D radiation pattern of each antenna Gain during Talk-Mode.
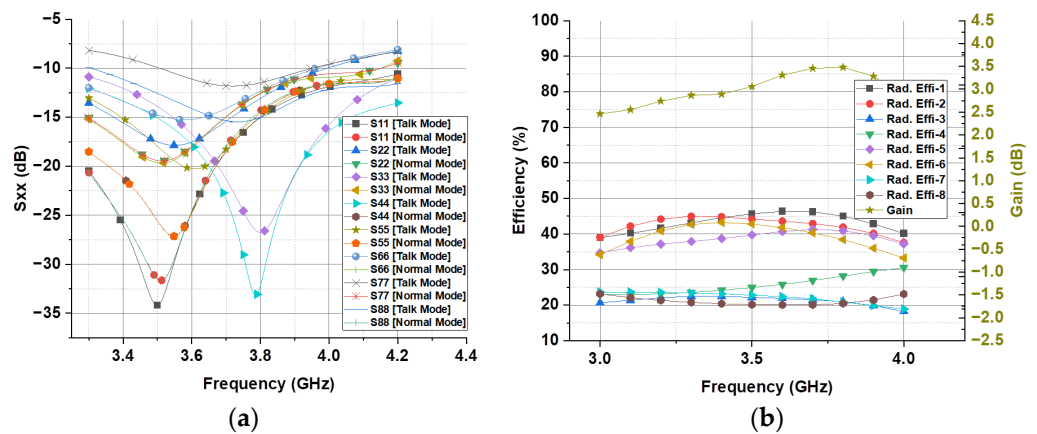
Figure 20. Performance parameter of MIMO array during Talk-mode. (**a**) Reflection coefficients, (**b**) Total efficiency and Gain.

5. Conclusions

The proposed antenna design offers a compact and efficient solution for enabling 5G NR connectivity in mobile devices operating in the sub-6 GHz frequency range, specifically targeting the n77 (3.3–4.2 GHz) and n78 (3.3–3.8 GHz) bands defined in the 3GPP Release 15 and Release 16 specifications. With its wideband characteristics spanning the entire 3.3 GHz to 4.2 GHz range, the developed antenna is well-suited for integration into 5G

mobile handsets. The antenna design incorporates an innovative configuration comprising eight circular microstrip edge-fed patches arranged in an orthogonal configuration with an octagonal slot etched into the ground plane and a neutral line among the feed lines of adjacent orthogonally polarized patches. This intricate geometry yielded exceptional performance characteristics, including a realized gain of up to 4 dBi, remarkable port-to-port isolation below -18 dB across the targeted frequency band, an exceptionally low envelope correlation coefficient under 0.01, and a high radiation efficiency exceeding 80%. The simulated results were thoroughly validated through comprehensive measurements conducted on the fabricated antenna array prototype, demonstrating an excellent correlation between theoretical predictions and empirical observations. Furthermore, the article presented a comprehensive evaluation of the array's performance under realistic operating conditions, investigating the impact of grip and talk modes on the antenna's behavior. This analysis provides invaluable insights into the design's suitability for practical mobile device integration, ensuring robust and reliable performance in real-world scenarios. Future work could involve integrating the proposed MIMO antenna design into 5G small-cell systems, enabling efficient implementation in future 5G small-cell deployments. Additionally, exploring the antenna's performance in massive MIMO configurations and evaluating its suitability for emerging 6G technologies would be valuable research directions.

Author Contributions: Conceptualization, A.A.K. and Z.W.; Methodology, A.A.K.; Software, D.L. and A.A.; Validation, Z.W. and D.L.; Formal analysis, D.L. and A.A.; Investigation, A.A.K.; Resources, Z.W.; Writing—original draft, A.A.K.; Writing—review & editing, Z.W.; Supervision, Z.W. All authors have read and agreed to the published version of the manuscript.

Data Availability Statement: The data used to support the findings of this study are included within the article.

Conflicts of Interest: Author Ali Ahmed was employed by the company ACES (Advanced Communications & Electronics Systems). The remaining authors declare that the research was conducted in the absence of any commercial or financial relationships that could be construed as a potential conflict of interest.

Abbreviations

MIMO	Multiple-input multiple-output
FR-4	Flame retardant 4
PCB	Printed circuit board
FR1	Frequency range 1
NR	New radio
ECC	Envelop correlation coefficient
TARC	Total active reflection coefficient
RF	Radio frequency
CST	Computer simulation technology
3GPP	Third generation partnership project
IoT	Internet of Things
ORAN	Open radio access network

References

1. Chataut, R.; Akl, R. Massive MIMO systems for 5G and beyond networks—Overview, recent trends, challenges, and future research direction. *Sensors* **2020**, *20*, 2753. [CrossRef] [PubMed]
2. Rajoria, S.; Trivedi, A.; Godfrey, W.W. A comprehensive survey: Small cell meets massive MIMO. *Phys. Commun.* **2018**, *26*, 40–49. [CrossRef]
3. Parchin, N.O.; Basherlou, H.J.; Al-Yasir, Y.I.; Abd-Alhameed, R.A.; Abdulkhaleq, A.M.; Noras, J.M. Recent developments of reconfigurable antennas for current and future wireless communication systems. *Electronics* **2019**, *8*, 128. [CrossRef]

4. Parchin, N.O.; Al-Yasir, Y.I.A.; Abd-Alhameed, R.A. A compact 5G antenna array with ultra-wide bandwidth for mm-wave smartphone applications. In Proceedings of the 15th European Conference on Antennas and Propagation (EuCAP), Dusseldorf, Germany, 22–26 March 2021.

5. Hussain, R.; Sharawi, M.S. 5G MIMO antenna designs for base station and user equipment: Some recent developments and trends. *IEEE Antennas Propag. Mag.* **2021**, *64*, 95–107. [CrossRef]

6. Brand, P.; Falk, J.; Sue, J.A.; Brendel, J.; Hasholzner, R.; Teich, J. Adaptive predictive power management for mobile LTE devices. *IEEE Trans. Mob. Comput.* **2020**, *20*, 2518–2535. [CrossRef]

7. Ullah, A.; Parchin, N.O.; Abdul-Al, M.; Santos, H.M.; See, C.H.; Hu, Y.F.; Abd-Alhameed, R.A. Internal MIMO antenna design for multi-band mobile handset applications. In Proceedings of the 2021 29th Telecommunications Forum (TELFOR), Belgrade, Serbia, 23–24 November 2021; pp. 1–4.

8. Parchin, N.O.; Basherlou, H.J.; Alibakhshikenari, M.; Parchin, Y.O.; Al-Yasir, Y.I.; Abd-Alhameed, R.A.; Limiti, E. Mobile-phone antenna array with diamond-ring slot elements for 5G massive MIMO systems. *Electronics* **2019**, *8*, 521. [CrossRef]

9. Kiani, S.H.; Altaf, A.; Anjum, M.R.; Afridi, S.; Arain, Z.A.; Anwar, S.; Khan, S.; Alibakhshikenari, M.; Lalbakhsh, A.; Khan, M.A.; et al. MIMO antenna system for modern 5G handheld devices with healthcare and high rate delivery. *Sensors* **2021**, *21*, 7415. [CrossRef] [PubMed]

10. Kiani, S.H.; Altaf, A.; Abdullah, M.; Muhammad, F.; Shoaib, N.; Anjum, M.R.; Damaševičius, R.; Blažauskas, T. Eight element side edged framed MIMO antenna array for future 5G smart phones. *Micromachines* **2020**, *11*, 956. [CrossRef] [PubMed]

11. Parchin, N.O.; Al-Yasir, Y.I.; Noras, J.M.; Abd-Alhameed, R.A. Dual-polarized MIMO antenna array design using miniaturized self-complementary structures for 5G smartphone applications. In Proceedings of the European Conference (EuCAP), Krakow, Poland, 31 March–5 April 2019; pp. 1–4.

12. Li, Y.; Sim, C.-Y.-D.; Luo, Y.; Yang, G. High-isolation 3.5 GHz eight-antenna MIMO array using balanced open-slot antenna element for 5G smartphones. *IEEE Trans. Antennas Propag.* **2019**, *67*, 3820–3830. [CrossRef]

13. Abdullah, M.; Altaf, A.; Anjum, M.R.; Arain, Z.A.; Jamali, A.A.; Alibakhshikenari, M.; Falcone, F.; Limiti, E. Future smartphone: MIMO antenna system for 5G mobile terminals. *IEEE Access* **2021**, *9*, 91593–91603. [CrossRef]

14. Younas, T.; Zhao, Y.; Jeon, G.; Farid, G.; Tahir, S.; Mekonnen, M.; Shen, J.; Gao, M. A Framework to Connect IoT Edge Networks through 3D Massive MIMO. *Wirel. Netw.* **2023**, 1–11.

15. Younas, T.; Xing, X.; Shen, J.; Tahir, S.; Mekonen, M.; Gao, M. 3D Massive MIMO with Massive Connectivity for Internet of Things Devices. *Wirel. Netw.* **2023**, 1–12.

16. Long, D.; Wu, Q.; Fan, Q.; Fan, P.; Li, Z.; Fan, J. A power allocation scheme for MIMO-NOMA and D2D vehicular edge computing based on decentralized DRL. *Sensors* **2023**, *7*, 3449. [CrossRef] [PubMed]

17. Pandey, A. *Practical Microstrip and Printed Antenna Design*; Artech House: Norwood, MA, USA, 2019.

18. Parchin, N.O.; Al-Yasir, Y.I.A.; Basherlou, H.J.; Abd-Alhameed, R.A. A closely spaced dual-band MIMO patch antenna with reduced mutual coupling for 4G/5G applications. *Prog. Electromagn. Res. C* **2020**, *101*, 71–80. [CrossRef]

19. Diman, A.A.; Karami, F.; Rezaei, P.; Amn-e-Elahi, A.; Mousavirazi, Z.; Denidni, T.A.; Kishk, A.A. Efficient SIW-feed network suppressing mutual coupling of slot antenna array. *IEEE Trans. Antennas Propag.* **2021**, *69*, 6058–6063. [CrossRef]

20. Goud, J.R.; Rao, N.V.K.; Prasad, A.M. Design of triple band U-slot MIMO antenna for simultaneous uplink and downlink communications. *Prog. Electromagn. Res. C* **2020**, *106*, 271–283. [CrossRef]

21. Wang, C.; Wang, H.; Wu, P.; Hou, M. Dual-band closed-slot MIMO antenna for terminal wireless applications. *IEEE Trans. Antennas Propag.* **2022**, *70*, 6514–6525. [CrossRef]

22. Hussain, R.; Khan, M.U.; Sharawi, M.S. Dual-band Slot-Based MIMO Antenna Design with Independent Tuning. In Proceedings of the IEEE International Symposium on Antennas and Propagation and North American Radio Science Meeting, Montréal, QC, Canada, 5–10 July 2020.

23. Chang, K.; Hsieh, L.-H. *Microwave Ring Circuits and Related Structures*; John Wiley Sons: Hoboken, NJ, USA, 2004; Volume 156.

24. Batchelor, J.C.; Langley, R.J. Microstrip annular ring slot antennas for mobile applications. *Electron. Lett.* **1996**, *32*, 1635–1636. [CrossRef]

25. Alibakhshikenari, M.; Babaeian, F.; Virdee, B.S.; Aissa, S.; Azpilicueta, L.; See, C.H.; Althuwayb, A.A.; Huynen, I.; Abd-Alhameed, R.A.; Falcone, F.; et al. A Comprehensive Survey on Various Decoupling Mechanisms with Focus on Metamaterial and Metasurface Principles Applicable for SAR and MIMO Systems. *IEEE Access* **2020**, *8*, 192965–193004. [CrossRef]

26. Serghiou, D.; Khalily, M.; Singh, V.; Araghi, A.; Tafazolli, R. Sub-6 GHz dual-band 8×8 MIMO antenna for 5G smartphones. *IEEE Antennas Wirel. Propag. Lett.* **2020**, *19*, 1546–1550. [CrossRef]

27. Liu, R.; An, X.; Zheng, H.; Wang, M.; Gao, Z.; Li, E. Neutralization line decoupling tri-band multiple-input multiple-output antenna design. *IEEE Access* **2020**, *8*, 27018–27026. [CrossRef]

28. Saleh, A.M.; Nagim, T.A.; Abd-Alhameed, R.A.; Noras, J.M.; See, C.H. Mutual coupling reduction of dual-band uni-planar MIMO system using neutralization line technique. *Appl. Comput. Electromagn. Soc. J. (ACES)* **2020**, *35*, 176–186.

29. Birwal, A.; Singh, S.; Kanaujia, B.K.; Kumar, S. MIMO/diversity antenna with neutralization line for WLAN applications. *MAPAN* **2021**, *36*, 763–772. [CrossRef]

30. Radio, N. User Equipment (UE) Radio Transmission and Reception—Part 1: Range 1 Standalone (Release 16). 3GPP TS 38101-1-G30, Technical Specification 2020. Available online: https://www.etsi.org/deliver/etsi_ts/138100_138199/13810101/16.04.00_60/ts_13810101v160400p.pdf (accessed on 8 May 2024).

31. User Equipment. User Equipment (UE) Radio Transmission and Reception; Part 2: Range 2 Standalone. Part 1: Range 1 Standalone 2020. Available online: https://www.etsi.org/deliver/etsi_ts/138100_138199/13810102/16.04.00_60/ts_13810102v160400p.pdf (accessed on 8 May 2024).

32. Li, Y.; Yuan, M.; Jia, Y.; Zhai, H.; Liu, C. A compact four port MIMO antenna using connected neutral lines for enhanced isolation. In Proceedings of the 2021 International Conference on Microwave and Millimeter Wave Technology (ICMMT), Nanjing, China, 23–26 May 2021; pp. 1–3.

33. Elfergani, I.; Hussaini, A.S.; Rodriguez, J.; Abd-Alhameed, R. *Antenna Fundamentals for Legacy Mobile Applications and Beyond*; Springer: Berlin/Heidelberg, Germany, 2018; Volume 329.

34. Hu, W.; Liu, X.; Gao, S.; Wen, L.-H.; Qian, L.; Feng, T.; Xu, R.; Fei, P.; Liu, Y. Dual-band ten-element MIMO array based on dual-mode IFAs for 5G terminal applications. *IEEE Access* **2019**, *7*, 178476–178485. [CrossRef]

35. Al-Ani, N.M.K.; Al-Ani, O.A.S.; Mosleh, M.F.; Abd-Alhameed, R.A. A Dual-Polarized MIMO Array Antenna System for Future Smartphone. *J. Phys. Conf. Ser.* **2021**, *1804*, 012123. [CrossRef]

36. Chizhik, D.; Ling, J.; Samardzija, D.; Valenzuela, R.A. Spatial and polarization characterization of MIMO channels in rural environment. In Proceedings of the 2005 IEEE 61st Vehicular Technology Conference, Stockholm, Sweden, 30 May–1 June 2005; Volume 1, pp. 161–164.

37. Tiwari, R.N.; Singh, P.; Kanaujia, B.K.; Kumar, P. Compact circularly polarized MIMO printed antenna with novel ground structure for wideband applications. *Int. J. RF Microw. Comput. Aided Eng.* **2021**, *31*, e22737. [CrossRef]

38. Gao, C.; Li, X.-Q.; Lu, W.-J.; Wong, K.-L. Conceptual design and implementation of a four- element MIMO antenna system packaged within a metallic handset. *Microw. Opt. Technol. Lett.* **2018**, *60*, 436–444. [CrossRef]